Journal of Marine Research, 63, 497–527, 2005

Journal of
MARINE RESEARCH

Volume 63, Number 3

On rectification of randomly forced flows

by Pavel S. Berloff[1,2]

ABSTRACT

Nonlinear rectification of the ocean circulation driven by random forcing, which simulates the effect of unresolved eddies, is studied in an idealized closed basin. The results are based on the analysis of randomly forced solutions and linear eigenmodes. Depending on the forcing strength, two rectification regimes are found: zonal jets and isolated gyres. It is shown that both regimes are due to nonlinear interactions of resonant basin modes. In the zonal-jet regime, these interactions involve complex interplay between resonant baroclinic modes and some secondary modes. Both Rhines' scaling for zonal jets and prediction of gyres based on the maximum entropy argument are not confirmed.

1. Introduction

The principal phenomenon studied in this paper is nonlinear rectification of geostrophic turbulence driven by random forcing. The mesoscale eddy flux divergences of momentum and potential vorticity (PV) are capable of driving the large-scale oceanic currents. In the comprehensive ocean models, the eddies are typically not resolved and their effects are parameterized in terms of the turbulent diffusion. Recently, it has been shown that in the midlatitude oceanic gyres fluctuations of the eddy forcing drive strong rectified response (Berloff, 2005; hereafter, B05). In this context, rectification is the emergence of nonzero time-mean currents due to forces fluctuating around zero mean. The rectification is an anti-diffusive phenomenon, which can be modeled by adding random forcing to a nonlinear, non-eddy-resolving ocean model (B05). The random-forcing approach for

1. Department of Physical Oceanography, Woods Hole Oceanographic Institution, Woods Hole, Massachusetts, 02543, U.S.A. ***email: pberloff@whoi.edu***
2. DAMTP-CMS, University of Cambridge, Cambridge, CB3 0WA, United Kingdom.

modeling eddy effects is actively developed in various areas of fluid dynamics: in the contexts of the homogeneous and isotropic 3D turbulence (e.g., Herring and Kraichnan, 1971; Laval *et al.,* 2003) and linear dynamics (Farrell and Ioannou, 1995; Whitaker and Sardeshmukh, 1998; Zhang and Held, 1999; DelSole, 2001). The approach involves searching for the right model of the eddy effects, on the one hand, and studying different rectification phenomena, on the other hand. The idealized geophysical models are usually of two classes: periodic zonal channel (or the whole sphere) that represents an atmosphere, or closed basin that represents an ocean.

The zonal-channel works focus on the emergence of rectified zonal jets, such as those observed on Jupiter and other giant gas planets. In this case a substantial part of the small-scale forcing is due to convecting cells. Whitehead (1975) observed the phenomenon in a lab experiment and Williams (1978)—in solutions of the global, barotropic atmosphere. The corresponding theory has been developed in Rhines (1975) and Haidvogel and Rhines (1983) and a comprehensive review of the subject is in Rhines (1994). The jets are formed due to the inverse energy cascade, which is typical for the 2D geostrophic turbulence, and the beta term that creates strong anisotropy and channels a large fraction of the energy into zonal currents, thus creating a strongly anisotropic energy spectrum (e.g., Vallis and Maltrud, 1993; Chekhlov *et al.,* 1996). On the other hand, it is argued that the jets can be a weakly nonlinear phenomenon (Manfroi and Young, 1999; 2002). It has been suggested that the rectified jets form if the planetary vorticity gradient exceeds a critical threshold; that is, below some critical latitude which depends on the Rossby deformation radius and the energy rate (Smith, 2004; Theiss, 2004). It is also argued that, with the latitude-dependent planetary-vorticity gradient, there is an equatorward energy cascade that should amplify rectified jets at low latitudes (Theiss, 2004). In the two-layer doubly periodic flow, the observed zonal scaling of the jets is found to be consistent with the one suggested by Rhines (Panetta, 1993). Recently, it has been shown that in the doubly periodic domain, barotropic dynamics generates a "saw-tooth" vorticity profile, thus confounding any scaling behavior of the statistical-equilibrium energy spectrum, and the resulting long-time average of the turbulent solution is not unique, depending on its initial state and evolution history (Danilov and Gurarie, 2004).

The closed-basin works focus on emergence of large-scale gyres. The statistical equilibrium mechanics predicts that, in the absence of forcing and dissipation, the barotropic-vorticity solutions evolve to the equilibrium state characterized by the time-mean westward flow in the interior of the basin and the inertial boundary layers near zonal boundaries (Salmon *et al.,* 1976). In the northern hemisphere this state is associated with the anticyclonic gyre in the north and its cyclonic counterpart in the south (Fofonoff, 1954). It is argued that this equilibrium remains valid in the situation with realistic forcing and friction given by the anticipated-vorticity formulation (Griffa and Salmon, 1989). Emergence of the Fofonoff gyres is found in different configurations of the barotropic dynamics (e.g., Griffa and Castellari, 1991; Seidov and Marushkevich, 1992). It is argued that in the no-slip barotropic case the gyres are prohibited and, hence, some other

rectification pattern has to form, because correlation between the relative vorticity and the latitude is always zero (Cummins, 1992; Wang and Vallis, 1994). Finally, it has been found that statistical details of random forcing—rarely analyzed and discussed—are qualitatively important for the dynamic response, therefore they must be physically constrained and more thoroughly studied (Treguier and Hua, 1987; Sura and Penland, 2002).

Even if in the upper ocean there is a phenomenon analogous to the zonal jets on giant gas planets, it is masked by the wind-driven currents. On the other hand, below the thermocline alternating zonal flows are observed with float measurements (Hogg and Owens, 1999) and in comprehensive eddy-resolving models (Nakano and Hasumi, 2005). Although, it is argued that some of the large-scale zonal currents are due to the wind stress pattern (Treguier *et al.,* 2003), dynamical origin of the finer-scale zonal jets is not clearly understood. In particular, the observed and modeled jets have a meridional scale that is substantially larger than the Rhines' scale, which may be an indication of dynamical processes different from those acting in atmospheres of giant gas planets. Recently, it has been suggested that Rossby waves and basin modes, and their instabilities are important aspects of forced turbulence in a closed basin (Cessi and Primeau, 2001; LaCasce, 2002; LaCasce and Pedlosky, 2002; 2004, hereafter: LP04). In this paper these results are extended and connected with the rectification phenomenon.

The main questions asked in this paper are the following:

(i) What are the generic rectification regimes in an idealized closed basin?
(ii) How do rectification patterns depend on physical parameters?
(iii) How can these patterns be explained in terms of fluid dynamics?

Below, Section 2 describes the ocean model and discusses some relevant dynamical mechanisms. Section 3 analyzes randomly forced solutions, Section 4 explains rectification in terms of the nonlinearly interacting basin modes, and Section 5 summarizes the results.

2. Ocean model and dynamical mechanisms

a. Idealized ocean model

The fluid-dynamic model represents the midlatitude ocean with prescribed density stratification in a flat-bottom square basin with north-south and east-west boundaries. The quasi-geostrophic (QG), potential-vorticity (PV) equations (Pedlosky, 1987) for $N = 3$ dynamically active isopycnal layers are:

$$\frac{\partial q_i}{\partial t} + J(\psi_i, q_i) + \beta \frac{\partial \psi_i}{\partial x} = f_i + \nu \nabla^4 \psi_i, \tag{1}$$

where i is the layer index starting from the top. The meridional planetary-vorticity gradient is β, the random forcing is f, and $J(,)$ is the horizontal Jacobian operator. The PV anomalies, q_i, are connected with the velocity streamfunctions, ψ_i, through the coupled elliptic equations:

$$\nabla^2\psi_i - (1 - \delta_{i,1})S_{i,1}(\psi_i - \psi_{i-1}) - (1 - \delta_{i,N})S_{i,2}(\psi_i - \psi_{i+1}) = q_i, \tag{2}$$

with the stratification parameters:

$$S_{i,1} = f_0^2\left(H_i g \frac{(\rho_i - \rho_{i-1})}{\rho_1}\right)^{-1}, \quad 1 < i \le N, \tag{3}$$

$$S_{i,2} = f_0^2\left(H_i g \frac{(\rho_{i+1} - \rho_i)}{\rho_1}\right)^{-1}, \quad 1 \le i < N, \tag{4}$$

where ρ_i and H_i are the fluid density and depth of the ith layer, and f_0 is the mid-basin Coriolis parameter. The horizontal velocity components are found as

$$u_i = -\frac{\partial\psi_i}{\partial y}, \quad v_i = \frac{\partial\psi_i}{\partial x}. \tag{5}$$

The basin is square with 3840 km size. On the lateral boundaries there is the no-slip boundary condition, that is, the velocity is zero, but in some cases the no-slip solutions are compared with the free-slip solutions, which have zero relative vorticity on the boundaries. Also, there is the mass conservation constraint for each layer:

$$\frac{\partial}{\partial t}\int\int (\psi_1(x, y) - \psi_2(x, y))\, dx\, dy = 0, \tag{6}$$

$$\frac{\partial}{\partial t}\int\int (\psi_3(x, y) - \psi_2(x, y))\, dx\, dy = 0. \tag{7}$$

In the three-layer case considered here, the isopycnal layer depths are $H_1 = 200$ m, $H_2 = 1200$ m, and $H_3 = 2600$ m starting from the top, the ratio of the density jumps across the layer interfaces is $\gamma = (\rho_2 - \rho_1)/(\rho_3 - \rho_2) = 2$, so that the first, Rd_1, and second, Rd_2, Rossby deformation radii are 52 and 30 km, respectively. The standard value of β is $\beta_0 = 2 \times 10^{-11}\ \mathrm{m^{-1}\ s^{-1}}$, except when β is varied. In the weak-forcing regime, the random-forcing variance, $\sqrt{\sigma_f}$, is varied around $\sqrt{\sigma_0} = 0.83 \times 10^{-3}\ \mathrm{days^{-2}}$, and in the strong-forcing regime it is 20 times larger than that. The choice of the forcing variance is motivated by B05, where large variance is found around the eastward-jet extension of the subtropical western boundary current, and weak variance is found elsewhere in the basin. The lateral viscosity coefficient, ν, is varied around $\nu_0 = 10^3\ \mathrm{m\ s^{-2}}$. The solution with σ_0, σ_0, and ν_0 is referred to as the standard solution. The horizontal grid resolution is uniform with 257×257 grid points, except for solutions with small ν and Rd_1, for which the resolution is doubled in each direction. The space-time correlated random forcing, f, is generated by the algorithm described in the Appendix. For simplicity f is limited to the upper isopycnal layer, where the observed eddy forcing is the strongest (B05). For each set of parameters, the model solutions are spun up for 100 years and then integrated over

another 100 years of interest. It is found that if another 100 years of integration are added, this has no significant effect on the rectified flow pattern.

b. Dynamical rectification mechanisms

There are two necessary conditions for rectification: nonlinearity of the dynamics and the β-effect. The simplest paradigm of the rectification is the emergence of zonal jets driven by spatially localized, oscillating forcing in the unbounded domain. Let's consider PV dynamics forced by the localized, zero-mean, external forcing, $\Phi(t, \mathbf{x})$, with (positive) amplitude A:

$$\frac{dq}{dt} + \beta v = A\Phi(t, \mathbf{x}). \tag{8}$$

Integrating (8) over a short time interval and multiplying the result with v gives:

$$\delta q v = \left(A \int \Phi \, dt - \beta \, \delta y \right) v. \tag{9}$$

In the weak-forcing situation ($A \to 0$) or away from the directly forced latitudes, (9) can be averaged over an ensemble of realizations. Taking into account that $v = \delta y/\delta t$, the meridional eddy q-flux is given by:

$$\langle \delta q v \rangle = -\frac{\beta}{2} \frac{d}{dt} \langle y^2 \rangle, \tag{10}$$

where the ensemble averaging is denoted by angular brackets. If there is irreversible Lagrangian dispersion of the fluid elements, then there is the asymptotic diffusive limit in which: $\langle y^2 \rangle \sim t$. In this limit the rhs of (10) is negative, hence the ensemble-average meridional flux of q, which is equivalent to the Eulerian flux of q, is negative. Since the flux has to decay to zero farther away from the forced latitudes, its divergence has to be positive/negative to the north/south of these latitudes, which is consistent with the induced broad, zonal westward currents decaying to the north and south. This argument explains the appearance of the westward rectified flow at the unforced latitudes in the localized-forcing situation (Whitehead, 1975; Haidvogel and Rhines, 1983). Overall, this flow regime is a result of the meridional mixing and partial homogenization of the absolute PV. In the case of the oscillating localized forcing, the mixing is driven by the Rossby waves radiating away from source.

The strong-forcing regime realizes when A is sufficiently large and v becomes significantly correlated with the forcing. In the near-Sverdup regime, that is, when the leading-order balance is between the forcing and the meridional advection of planetary vorticity, this correlation is positive: $\langle v \int \Phi \, dt \rangle > 0$. In this case the flux divergence pattern is opposite to the one described above, therefore it induces a narrow, zonal eastward jet occupying the forced latitudes. In the localized-forcing situation both dynamical regimes

coexist, and in a closed basin the flow rectification takes the form of an elongated recirculation dipole, with eastward jet in the middle, that extends from the western boundary to the forcing location.

If random-forcing variance is spatially homogeneous rather than localized, then the above regimes cannot exist because A is not negligible everywhere and the meridional q-flux cannot be positive everywhere. In this situation the third regime can occur, which is the resonance (Pedlosky, 1965). If L is basinscale and $T = [\beta L]^{-1}$ is timescale, then the relevant nondimensional parameter is

$$\epsilon = \frac{A}{\beta^2 L^2}, \tag{11}$$

and the governing dynamics scales as

$$\frac{\partial q}{\partial t} + v = -\epsilon \nabla \mathbf{u} q + \epsilon^2 (F + D), \tag{12}$$

where F and D indicate the forcing and dissipation terms. Given the formal expansion,

$$q = q_0 + \epsilon q_1 + o(\epsilon), \tag{13}$$

the resulting sequence of linear problems begins with:

$$\frac{\partial q_0}{\partial t} + v_0 = 0, \tag{14}$$

$$\frac{\partial q_1}{\partial t} + v_1 = -\nabla \mathbf{u}_0 q_0. \tag{15}$$

Thus, nonlinear self-interaction of resonant structures given by the leading-order dynamics, that is, rhs of (15), can be interpreted as an intrinsically generated forcing. Are there any resonant patterns in the randomly forced solutions? Can nonlinear interactions of these patterns induce observed rectified flows? These questions are addressed in the next two sections.

3. Rectification regimes

a. Weak-forcing regime

For a broad range of parameters, random forcing generates rectified elongated recirculations which are referred to here as alternating zonal jets (Fig. 1). The recirculations are zonally asymmetric—with more intense flow near the western boundary—which is due to reflection and dissipation of short Rossby waves (e.g., Pedlosky, 1987; see also Seidov and Marushkevich, 1992). This asymmetry is more pronounced in the deep ocean, because it is forced less intensively by the upper-ocean fluctuations. Here, it is found that the weaker the forcing the more confined the rectified flow is to the western boundary. In the interior of the

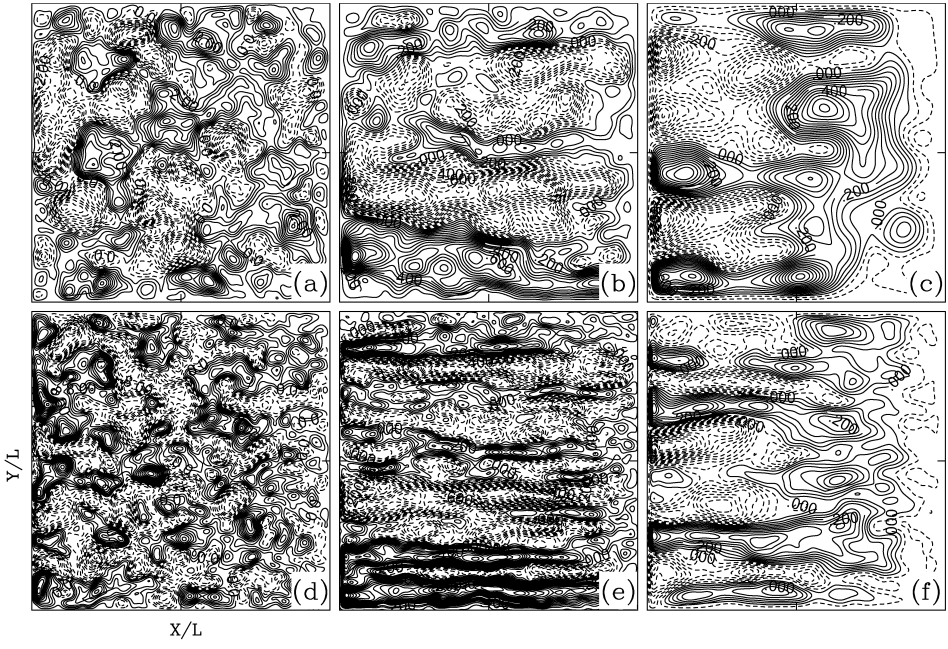

Figure 1. Velocity streamfunctions of the randomly forced solution with $\beta = .5\beta_0$ (the upper-branch regime in Fig. 2a): The upper-ocean (a) instantaneous and (b) time-mean patterns, and (c) the time-mean deep-ocean pattern. The lower row of panels shows the same quantities, but for the solution with $\beta = 4\beta_0$ (the lower-branch regime). In each layer, the streamfunctions are nondimensionalized by the maximum value of the corresponding $\langle\psi\rangle$. CIs are (a) 0.5, (b, c) 0.05, (d) 2.0, and (e, f) 0.05. The patterns in (b) and (e) have l_m equal to 670 and 280 km, respectively.

basin, the observed zonally-averaged rectified-velocity profile does not exhibit asymmetry between the eastward and westward jets, as it is found in the periodic channel (Panetta, 1993; Manfroi and Young, 1999). In the channel the westward jets are weaker and broader than the eastward jets. Also, the observed jets have no "saw-tooth" relative vorticity as it is found in the periodic channel (Danilov and Gurarie, 2004). Both the lack of the above asymmetries and the fact that the rectified jets in the closed basin are weak in comparison with the flow fluctuations suggest that in the basin the underlying dynamics is quite different from the atmospheric dynamics of the giant gas planets.

The most interesting structural property of the jets is their average meridional width, l_m. There are several theoretical predictions for l_m. Rhines' theory (Rhines, 1975) suggests that l_m is given by the scale L_R, at which advection of the planetary vorticity is balanced by advection of the PV anomaly:

$$L_R \equiv \left(\frac{U}{\beta}\right)^{1/2}, \tag{16}$$

where U is the velocity scale given by the variance of the flow fluctuations. Another similar scaling law,

$$L_{HH} \equiv \frac{\langle \nabla^2 \psi \rangle^{1/2}}{\beta}, \tag{17}$$

is based on the idea of the bounded, meridional Lagrangian lengthscale (Holloway and Hendershott, 1977; Ristorcelli and Poje, 2000). The above scalings do not take into account dissipation and stratification, and also they assume local dynamical balance. How does l_m in the randomly forced solutions scale with parameters of the problem? Here, l_m is defined as one half of the wavelength of the dominant spectral peak of the Fourier-decomposed, zonally averaged, time-mean velocity. An alternative method that defines l_m as the average distance between the neighboring zeros of the velocity (Ristorcelli and Poje, 2000) is found to be not robust.

The scaling laws (16) and (17) are checked by calculating several solutions with different β and σ_f (here, U is approximately proportional to $\sqrt{\sigma_f}$). Dependence of l_m on both ν and Rd_1 is studied as well. Overall, the above scaling laws are not confirmed, and actually no scaling laws are found for the large range of parameters (Fig. 2). The failure of (16) to explain the rectified jets is in agreement with its failure to explain the observed deep-ocean zonal jets (Treguier *et al.,* 2003). Instead of accurate scaling laws some approximate dependencies are found. Also, some critical parameter values are found at which l_m changes abruptly. These changes can be interpreted as transitions from one flow regime to another (e.g., Fig. 1 shows flow patterns for two distinct regimes with different l_m). Near the transition points the meridional Fourier spectra are bimodal, suggesting that the flow is actually a mixture of two regimes. In Section 4 it is argued that the discrete regimes can be attributed to different ensembles of the resonant basin modes.

With β varied from 0.125 to 8 times its standard value, two regime branches are found (Fig. 2a): the upper, small-β branch has l_m decreasing from 780 to 490 km, and the lower, large-β branch has l_m decreasing very little, from 277.7 to 275.6 km. The upper-branch, approximate power law, $l_m \sim \beta^{-0.2}$, implies much slower β-dependence than in the Rhines' scaling, and the lower branch has almost constant l_m. Near the critical parameter, with accuracy of 0.1β, no multiple regimes are found. The same two regimes are recovered by varying ν from 100 to 8000 $m^2\ s^{-1}$ (Fig. 2b). Overall, it is found that l_m substantially decreases with decreasing ν. In the context of weakly nonlinear barotropic dynamics with bottom drag, the dissipation rate is found to be important for the flow pattern (Manfroi and Young, 1999), and as dissipation gets stronger, l_m becomes smaller. This behavior is opposite to the present results. The difference is due to the scale-selective nature of the lateral dissipation that preferentially damps small-scale resonant basin modes that drive the rectification (Section 4). No robust dependence on Rd_1, which is varied from 26 to 1664 km, is found: with $Rd_1 = 26$ km the flow solution is on the upper branch, at 52 km it is on the lower branch, and for the larger values of Rd_1 there is another, intermediate-l_m regime (Fig. 2c). Finally, l_m shows almost negligible increase with $\sqrt{\sigma_f}$ (Fig. 2d), although

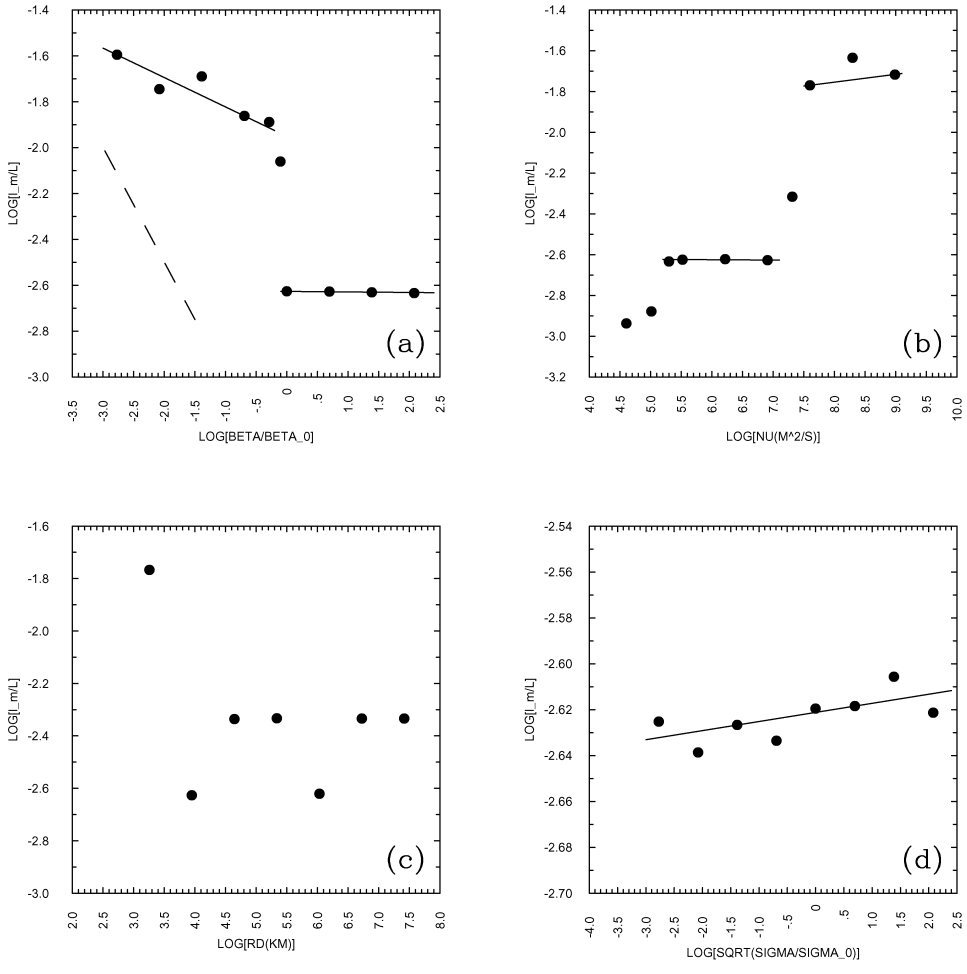

Figure 2. The average meridional widths, l_m, of the rectified jets as a function of (a) β, (b) ν, (c) Rd_1, and (d) σ_f. The Rhine's scaling in (a) is shown by the dashed line, and in (b) it would correspond to almost vertical line.

both the flow velocity and vorticity variances increase almost proportionally to $\sqrt{\sigma_f}$. This behavior is in sharp contrast with the power laws (16) and (17).

The Rhines' scaling law has been confirmed in a periodic channel (Panetta, 1993) with transient zonal jets, but it has never been examined in a closed basin. Here, the focus is on the time-mean rather than transient jets, therefore failure of (16) to predict l_m is not very surprising, given that any local balance does not necessarily yield a prediction of structure with long-range meridional correlations. Apparently, discreteness of l_m, insensitivity to the forcing variance (in the range of interest), and sensitivity to the viscosity require a dynamical explanation. At this point the *central hypothesis* of this study is formulated: the

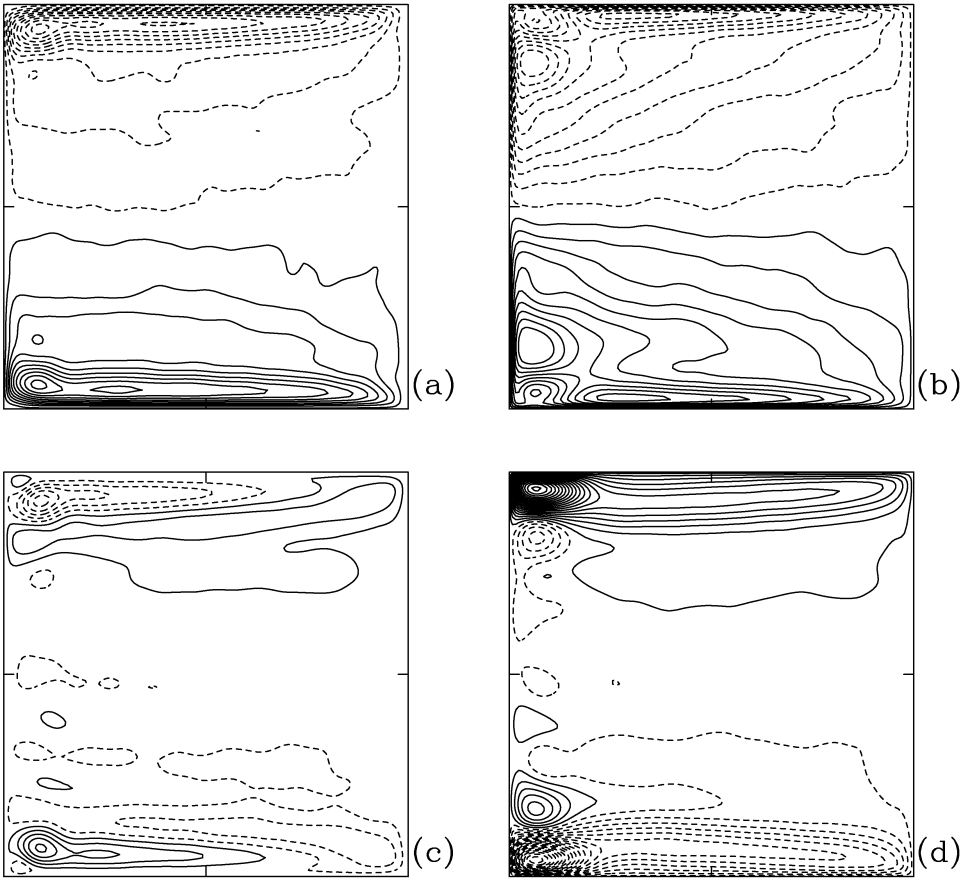

Figure 3. The upper-ocean rectified velocity streamfunction in the strong-forcing regime with the (a) no-slip and (b) free-slip boundary conditions. The lower row of panels shows the same, but for the deep ocean. The streamfunctions are non-dimensionalized by the maximum value of the no-slip $\langle\psi_1\rangle$. CIs are 0.1 and 0.2 in the upper and deep ocean panels, respectively.

flow rectification is controlled by the resonant basin modes and their nonlinear interactions; the modes are meridionally structured, therefore different ensembles of the modes drive different rectified regimes. In Section 3c some of these modes are diagnosed from the flow solutions, and in section 4 the linear eigenmodes are computed and systematically analyzed.

b. Strong-forcing regime

When σ_f is increased by the factor of 20, the elongated, cyclonic and anticyclonic gyres adjacent to the northern and southern boundaries (Fig. 3), respectively, dominate the upper-ocean rectified flow. This result holds when the no-slip boundary condition is

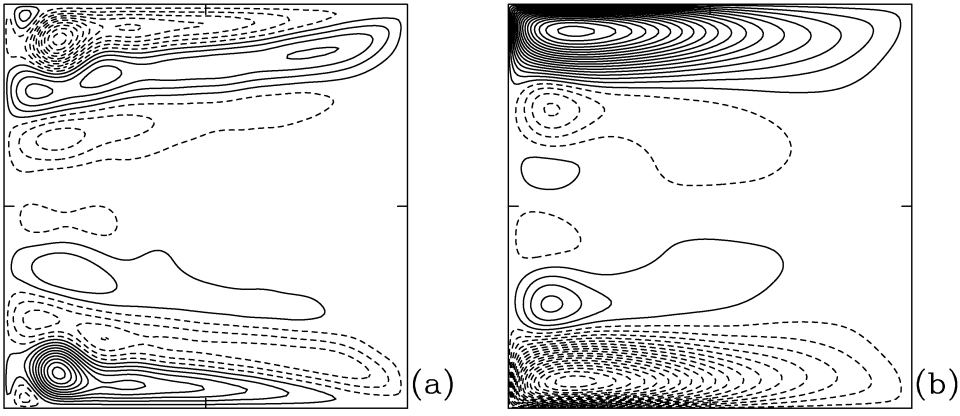

Figure 4. The barotropic rectified velocity streamfunction in the strong-forcing regime with the (a) no-slip and (b) free-slip boundary conditions. The streamfunctions are non-dimensionalized by the maximum value of the no-slip $\langle\psi\rangle$. CIs are (a) 0.1 and (b) 0.4.

replaced with the free-slip one, and in this case the gyres even invade the interior of the basin. In the deep ocean the no-slip rectification consists of the weak counter-rotating, elongated recirculations near each zonal boundary, and the free-slip rectification is in the form of the strong gyres occupying the northern and southern parts of the basin and rotating in the opposite way to the upper-ocean rectification. The upper-ocean circulation is exactly opposite to the Fofonoff gyres (Fofonoff, 1954) predicted by the equilibrium statistical mechanics argument of maximum entropy (Salmon *et al.,* 1976), therefore it is referred to here as the anti-Fofonoff gyres. In Section 4a the anti-Fofonoff flow pattern is explained by the upper-ocean nonlinear interactions of the resonant, weakly damped, baroclinic basin modes. The strong-forcing regime can be relevant to the ocean: in the eddy-resolving solutions of the oceanic gyres (B05) it manifests itself in terms of relatively weak, zonally elongated recirculations on the northern and southern flanks of the subpolar and subtropical gyres, respectively.

Barotropic, no- and free-slip randomly forced solutions (Fig. 4) are calculated and compared with the baroclinic solutions. The no-slip barotropic solution is characterized by weak recirculations, whereas the free-slip solution is dominated by strong Fofonoff-like gyres. Visual comparison of Figures 3c, d and 4 suggests that the deep-ocean rectification is dominated by the barotropic component. Why are the no- and free-slip barotropic rectifications so different? It can be shown (integrating by parts) that, with the no-slip boundary condition, correlation between latitude and barotropic PV, which is equivalent to the relative vorticity, is zero (Wang and Vallis, 1994):

$$C \equiv \int\int y\nabla^2\psi \, dxdy = 0. \tag{18}$$

This global constraint implies that either relative vorticity (in each of the Fofonoff or anti-Fofonoff gyres) is balanced by the opposite-sign relative vorticity concentrated in the viscous boundary layers or the gyres simply do not form. The latter is true for the no-slip barotropic mode. The free-slip case is not constrained by (18), and the resulting Fofonoff-like flow is consistent with the statistical-equilibrium mechanics arguments. On the other hand, the Fofonoff-like flow configuration is consistent with the phenomenon of rectified western flow driven by mixing of the background planetary-vorticity gradient (Section 2b) that is induced by resonant barotropic basin modes. Nonlinear interactions of these modes can also contribute to the rectification, but they are found to be very weak (Section 4a).

c. Diagnosed basin modes

What is the explanation for the failure of Rhines' scaling and the existence of discrete regimes? Here it is argued that l_m is set by nonlinear interactions of large-scale, propagating basin modes—this is a fundamentally non-local process, which breaks down both local dynamical balances and scalings based upon them. The Empirical Orthogonal Function (EOF) data analysis method (Preisendorfer, 1988) is used here to detect resonant basin modes. The method is applied to the standard solution, computed for 300 years, sampled every 50 days on a 65×65 uniform grid, and moderately filtered in space. The 10 leading EOFs are found as eigenvectors of the covariance matrix of ψ_1 fluctuations, and the corresponding Principal Components (PCs) are obtained by projecting the data on the eigenvectors. The leading EOF pair (Fig. 5) contains about 27% of the total variance and represents a single-cell basin-scale pattern. The EOFs are time-lag correlated, hence they describe a coherent propagating signal. The vertical structure of the EOFs is dominated by the second baroclinic mode. The phase speed of the pattern is westward, and the corresponding period, which is about 7 years, can be characterized as the transit time required to cross the basin. With the phase speed $C \approx -\beta R d_2^2$, a free second-baroclinic Rossby wave crosses the basin for 6.9 years, which is in close agreement with the observed period. The rest of the signal is dominated by the second EOF pair (Fig. 6) that represents a propagating two-cell pattern characterized by 21% of the total variance, and a time period of about 3.5 years. Are the diagnosed structures related to the basin modes?

Calculations of viscous basin modes have been made recently by Cessi and Primeau (2001), and it has been shown that the largest-scale modes are weakly damped and, therefore, can be easily excited (e.g., by random forcing, as in Cessi and Louazel, 2001). In Section 4 the modes are found as the eigenvalue solutions of the linearized dynamics and analyzed in detail, but this requires coarsening of the horizontal grid. Here the modes are diagnosed approximately by turning off the random forcing, integrating the ocean model in the decaying-flow regime, and calculating the corresponding EOFs. Given some initial adjustment, this method works well because the modes decay slowly. The method yields approximations of the first 3 modes given by the first 3 EOF pairs. The leading mode is shown in Figure 7: it looks like the resonant pattern in Figure 5, both in terms of the spatial structure and frequency. The e-folding timescale of the decay is about 50 years for the first

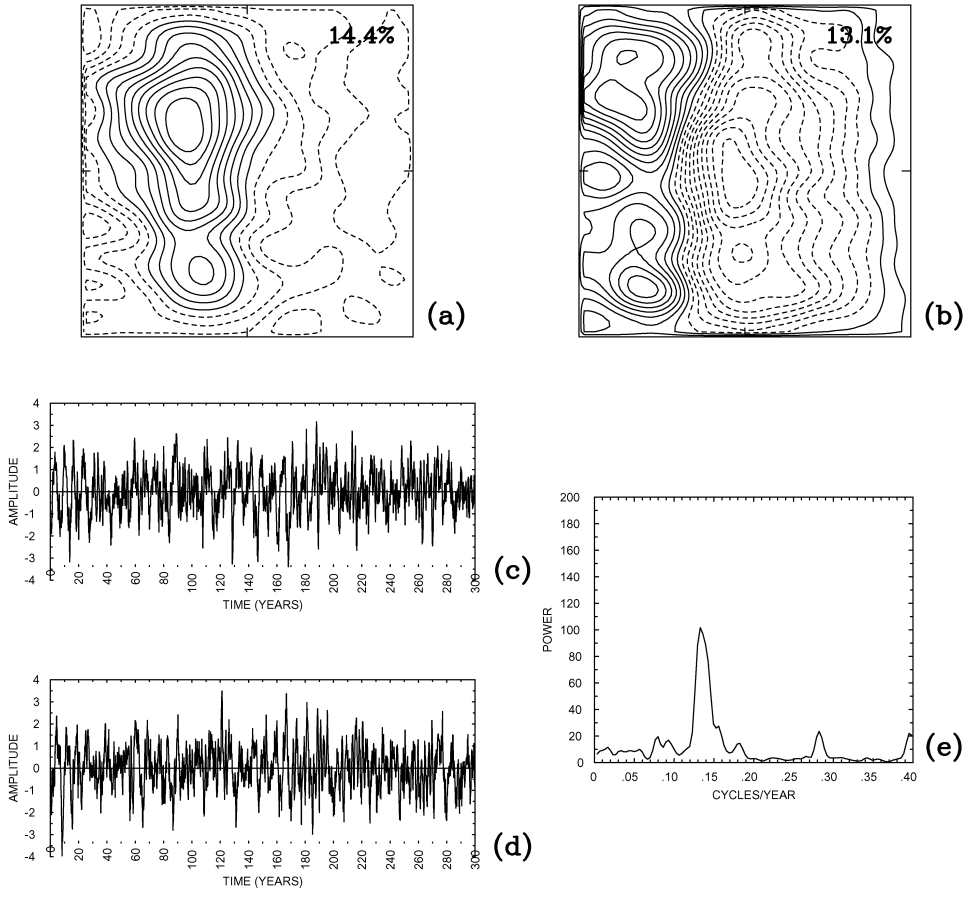

Figure 5. (a, b) The leading EOF pair of the space-filtered and subsampled, upper-ocean velocity streamfunction of the standard solution. The patterns are nondimensionalized by their maximum absolute values (CI is 0.1). The percentage fractions of the total variance are indicated. (c, d) The corresponding principal components (nondimensionalized by their variance) of the EOFs, and (e) the power frequency spectrum of the first component.

basin mode, and the second mode decays about twice as fast. Thus, the coherent patterns diagnosed from the randomly forced solution are indeed the resonant large-scale basin modes. Even if these modes are baroclinically unstable, as suggested in LP04, this instability has to be rather weak, because otherwise the modes would not have been diagnosed with such a clarity. The modes would be particularly vulnerable to the baroclinic instability if their transit times were long compared to the e-folding time of the instability. On the other hand, in Section 4b it is shown that the least stable but still weakly damped, secondary linear eigenmodes of the weakly damped, finite-amplitude, background basin modes do not have to be unstable in order to imprint their structure on the rectified flow.

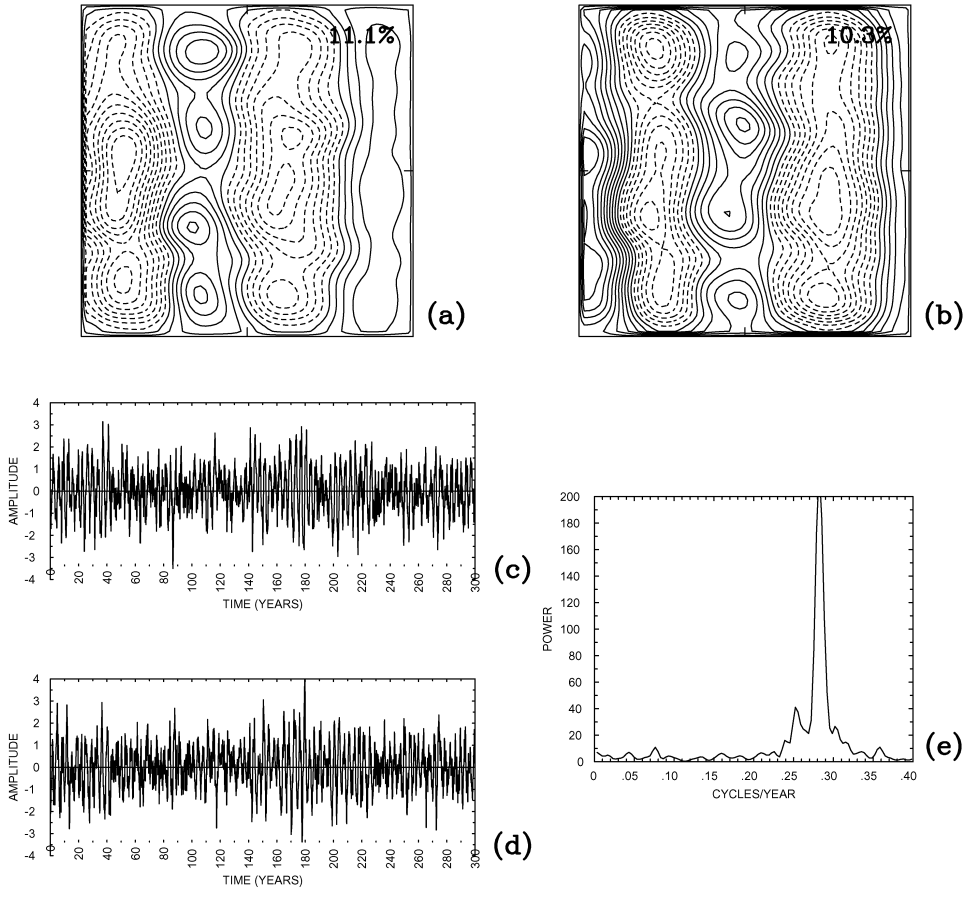

Figure 6. The same as in Figure 5, but for the second leading EOF pair.

This statement is analogous to saying that the basin modes themselves do not have to be unstable in order to be excited by the random forcing. It is found here that the weaker is the forcing, the more pronounced are the excited basin modes relative to other fluctuations.

4. Analysis of the basin modes

In the inviscid barotropic case and with $\psi = 0$ on the boundaries, the basin modes, that is, the eigenmodes of the linearized equations of motion, have a simple analytical expression (Pedlosky, 1987):

$$0 < x < 1,\ 0 < y < 1, \quad \omega_{mn} = -\frac{(2\pi)^{-1}\beta}{(m^2 + n^2)^{1/2}} \tag{19}$$

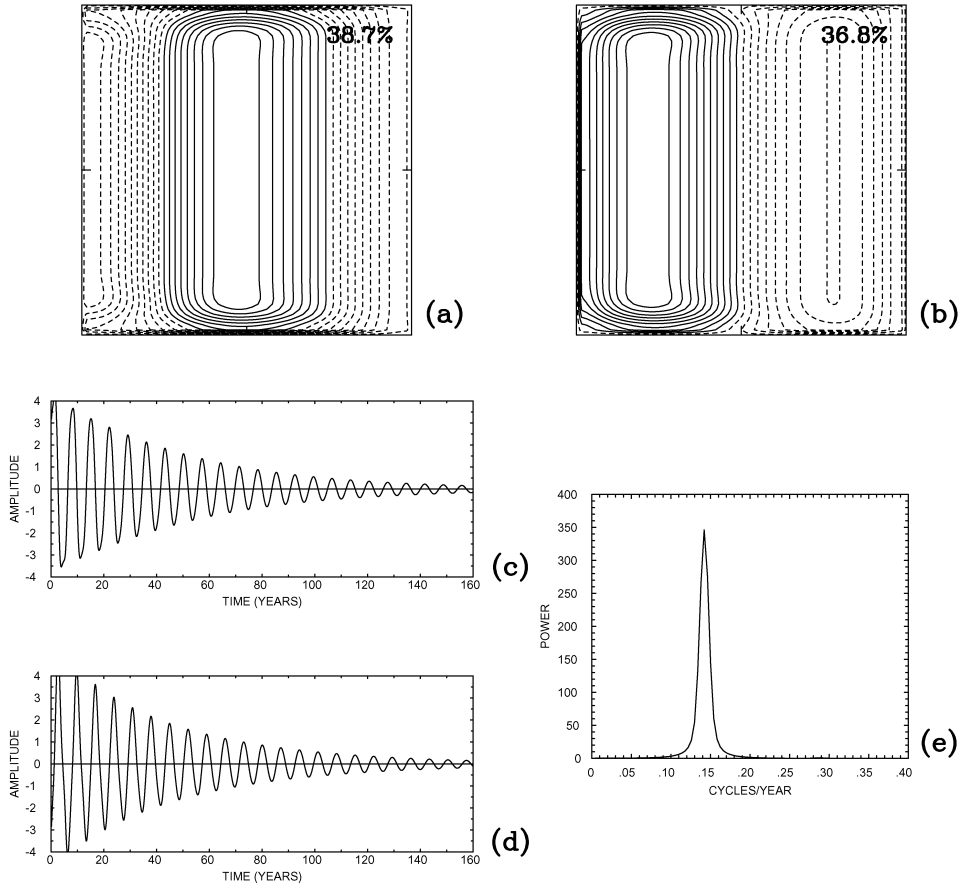

Figure 7. The same as in Figure 5, but for the decaying, unforced flow solution.

$$\psi = \cos\left[\frac{\beta x}{2\omega_{mn}} + \omega_{mn} t\right] \sin(m\pi x)\sin(n\pi y), \tag{20}$$

where ω_{mn} are the eigenfrequencies. The basin modes found and analyzed in this section are an extension of (19)–(20) for the situation with multi-layer stratification, viscous damping, integral mass constraint, and non-zero background flows.[3]

a. Eigenmodes with zero-background flow

Formally, the basin modes are the normal-mode solutions of the linearized governing equation (1), and Eqs. (2) and (6)–(7). Given the spectral transformation,

3. Recently, similar classes of such modes have been studied in the 1.5-layer situation (Cessi and Primeau, 2001; LaCasce and Pedlosky, 2002), and it has been suggested that the corresponding finite-amplitude modes can be vulnerable to the baroclinic instability.

$$\psi \rightarrow \psi(x, y)e^{-i\omega t}, \tag{21}$$

where $\omega = \omega_r + i\omega_i$, the linear problem is written in terms of 3 differential and 2 integral equations:

$$i\nu\nabla^4\psi_1 - i\beta\frac{\partial\psi_1}{\partial x} = \omega(\nabla^2\psi_1 + S_1(\psi_2 - \psi_1)) \tag{22}$$

$$i\nu\nabla^4\psi_2 - i\beta\frac{\partial\psi_2}{\partial x} = \omega(\nabla^2\psi_2 + S_{21}(\psi_1 - \psi_2) + S_{22}(\psi_3 - \psi_2)) \tag{23}$$

$$i\nu\nabla^4\psi_3 - i\beta\frac{\partial\psi_3}{\partial x} = \omega(\nabla^2\psi_3 + S_3(\psi_2 - \psi_3)) \tag{24}$$

$$0 = \omega\iint(\psi_1 - \psi_2)\,dx\,dy \tag{25}$$

$$0 = \omega\iint(\psi_3 - \psi_2)\,dx\,dy. \tag{26}$$

In the matrix form this system of equations can be written as the general eigenproblem:

$$\mathbf{A}\Psi = \omega\mathbf{B}\Psi \quad or \quad \mathbf{B}^{-1}\mathbf{A}\Psi = \omega\Psi, \tag{27}$$

where $\mathbf{A}$ and $\mathbf{B}$ are the linear-dynamics matrices, Ψ is an eigenvector solution, and ω is the corresponding eigenvalue. Here, (27) is solved numerically by discretizing the equations with the second-order finite differences on the uniform grid with 97×97 nodes. A very useful technical trick was to rewrite (22)–(26) in terms of the vertical modes, which are the barotropic, and the first and second baroclinic. With this rearrangement, (27) can be solved as three distinct eigenproblems of the smaller size. Here, the linear-algebra eigenvalue problem is solved directly with EISPACK subroutines. After the eigenvalue problem is solved, all of the eigenmodes are normalized by the energy norm (Pedlosky, 1987).

Nonlinear self-interaction of a basin mode,

$$F = -\nabla\mathbf{u}q, \tag{28}$$

can be viewed as intrinsically generated eddy forcing. Potentially, both time-mean,[4] $\langle F\rangle$, and fluctuation, F', components of F can drive rectifications, but here, given the two arguments below, the focus is on $\langle F\rangle$ only. First, history of the eddy PV flux divergence has been diagnosed from some of the weakly forced solutions of Section 3. This history has been applied as the only external forcing acting on the full dynamics, and the random forcing has been turned off. Comparison between this solution and two other solutions,

4. Here, it is equivalent to time average over an eigenperiod.

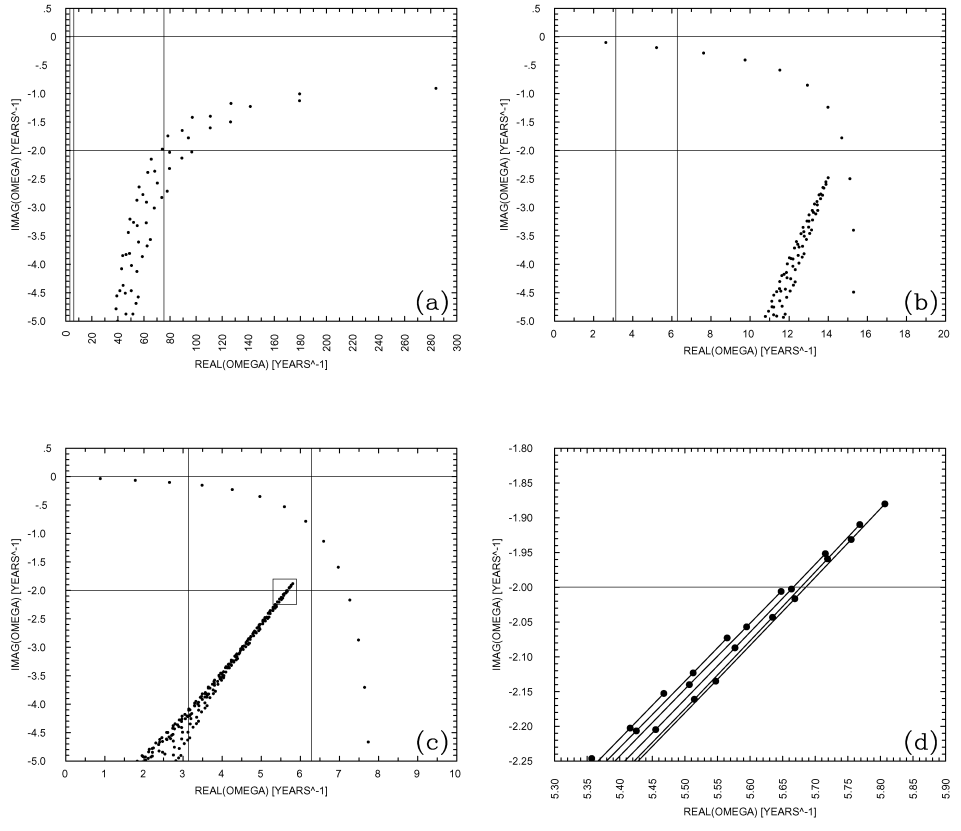

Figure 8. Eigenspectra of the (a) barotropic, (b) first baroclinic, and (c) second baroclinic eigenmodes. The vertical lines indicate the values of ω_r corresponding to the periods of 2 and 1 years, and of 1 month. The horizontal lines indicate $\omega_i = 0$ and -2 years^{-1} (i.e., no decay and the exponential decay over 0.5 years). Panel (d) zooms out part of the second-baroclinic eigenspectrum indicated by the small rectangular in panel (c). The lines in (d) connect eigenvalues corresponding to the eigenmodes with the same meridional wavenumber ($n = 2, 3, \ldots, 7$ starting from the right).

driven by either time-mean or fluctuation components of the history has shown that the rectified jets are completely dominated by $\langle F \rangle$. Second, similar analysis has been made for nonlinear interactions of some of the basin modes discussed in this section, and it is also found that $\langle F \rangle$ dominates.

The eigenspectrum of the eigenproblem (Fig. 8 shows only positive ω_r, because the eigenspectrum is symmetric with respect to the imaginary axis) contains three classes of the eigenmodes. The *MU-BCL*1- and *MU-BCL*2-modes are the meridionally unstructured, first and second baroclinic modes with the eigenvalues organized along curves connecting regions with small-ω_r/large-ω_i and large-ω_r/small-ω_i (Figs. 8b, c). The least damped *MU-BCL*2-mode (Fig. 9) corresponds to the diagnosed pattern in Figure 5 and the second

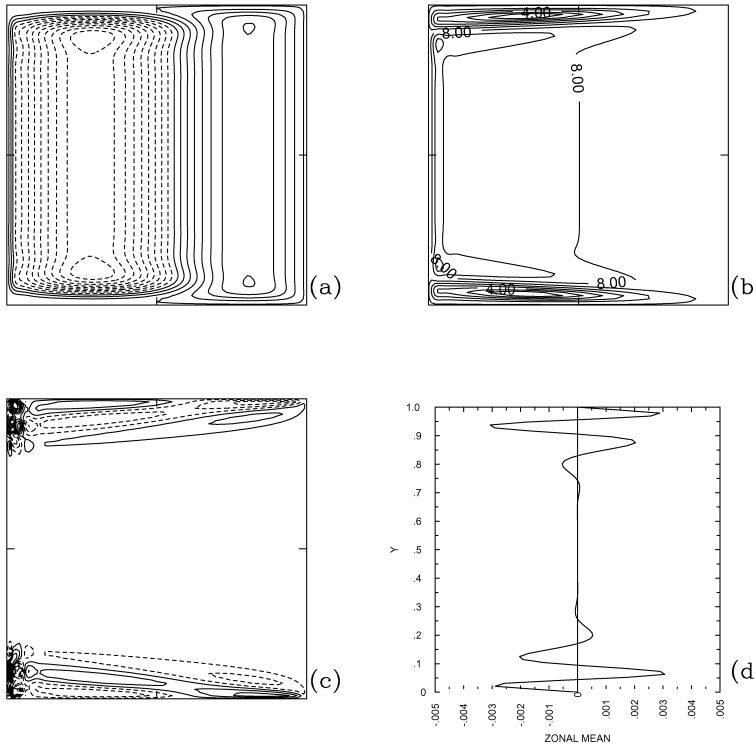

Figure 9. The least damped, second baroclinic mode: (a) real part, (b) amplitude, (c) upper-ocean eddy forcing, and (d) zonal mean of the upper-ocean eddy forcing. CIs are 1.0 in (a) and (b), and 0.01 in (c).

least damped *MU-BCL*2-mode (not shown) corresponds to the diagnosed pattern in Figure 6. The third least damped *MU-BCL*2-mode explains the third propagating coherent pattern, but beyond that the EOF technique combined with spatial filtering fails to recognize the presence of resonant basin modes, which doesn't imply that the modes are not excited. Thus, most of the large-scale variability in randomly forced solutions is well described by a few eigenmodes. The *MU-BCL*-modes consist of plane Rossby waves in the interior of the basin and boundary-layer corrections near the lateral boundaries (Figs. 9 and 10). As noted in LaCasce and Pedlosky (2002), such modes satisfy the boundary condition, $\psi(\Gamma) = \psi(t)$, without the need for short Rossby waves near the meridional boundaries. The small contribution of the short waves to the modes with just a few cells in the zonal direction results in the weak damping of the modes.

Eddy forcing of the *MU-BCL*-modes is significant only near the zonal boundaries, and only there can it contribute to the rectified jets pattern. However, in the interior of the basin the eddy forcing is weak, therefore it cannot fully account for the observed jets. The integral of the upper-ocean eddy forcing over the southern half of the basin,

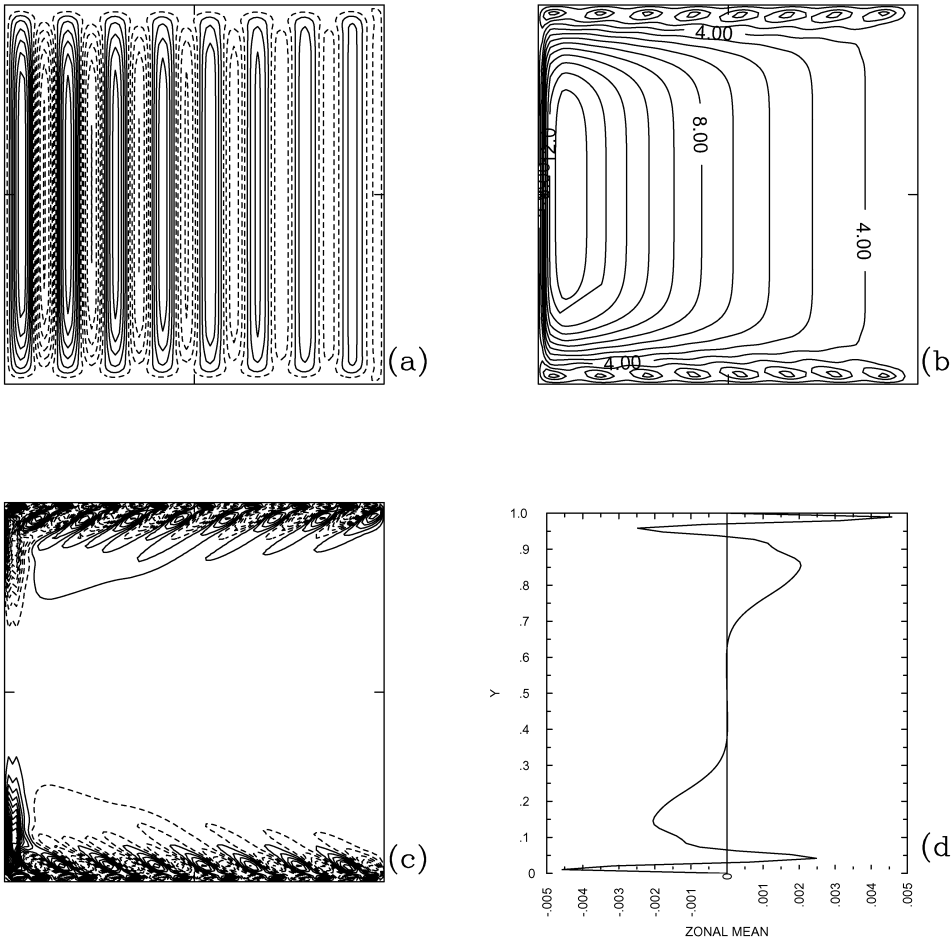

Figure 10. The same as Figure 9, but for the eighth least damped mode. CIs are (a) 2.0, (b) 1.0, and (c) 0.02.

$$F_{int} = \int_0^L \int_0^{L/2} \langle F_1 \rangle \, dx \, dy, \tag{29}$$

is negative for all of the *MU-BCL*-modes (Fig. 12b, c). This suggests that the modes, through their nonlinear self-interactions, tend to spin up an anticyclonic recirculation near the southern boundary. By the symmetry argument, these modes have to spin up a cyclonic recirculation near the northern boundary. Thus, it is argued here that the anti-Fofonoff upper-ocean flow pattern in the strong-forcing regime (Section 3b) is driven by the *MU-BCL*-modes. This result is not sensitive to replacing the no-slip lateral boundary condition with the free-slip condition, as implied by the flow pattern in Figure 3b. This is

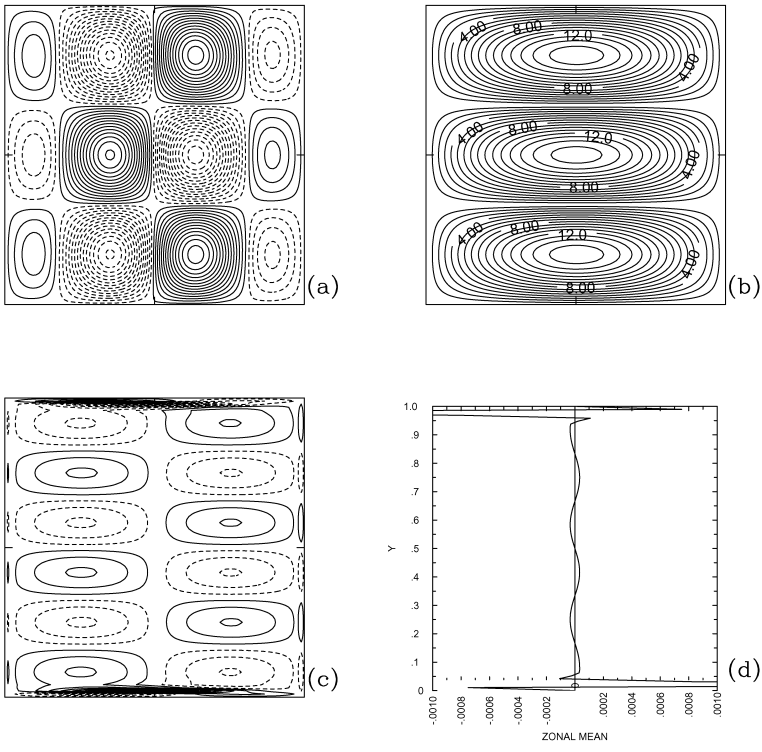

Figure 11. The fourth least damped, barotropic mode: (a) real part, (b) amplitude, (c) upper-ocean eddy forcing, and (d) zonal mean of the upper-ocean eddy forcing. CIs are 1.0 in (a) and (b), and 0.001 in (c).

confirmed by analysis of the free-slip *MU-BCL*-modes, not shown here for the sake of brevity, which also have positive F_{int}.

The second class of the eigenmodes are the fast, barotropic modes (*BT*-modes), like the one shown in Figure 11. Most of these modes are meridionally structured, thus they can contribute to the rectified zonal jets. However, the modes have very weak eddy forcing amplitudes, therefore they are not the main source of the rectified jets. The *BT*-modes have positive F_{int} (Fig. 12a) due to the eddy forcing spikes in the zonal boundary layers. This might suggest that the modes tend to drive Fofonoff-like gyres near the zonal boundaries, but such behavior is prohibited by the global constraint (18). This constraint is consistent with the alternating jets seen in the barotropic component of the weak-forcing regime, with the rectified pattern emerging in the strong-forcing regime (Fig. 4a), and with the deep-ocean rectification (Fig. 3c), which is dominated by the barotropic modes. It is easy to see that either with the free-slip condition or for the full PV anomaly, which has the stretching-term contribution, C doesn't have to be zero. The latter is associated with the

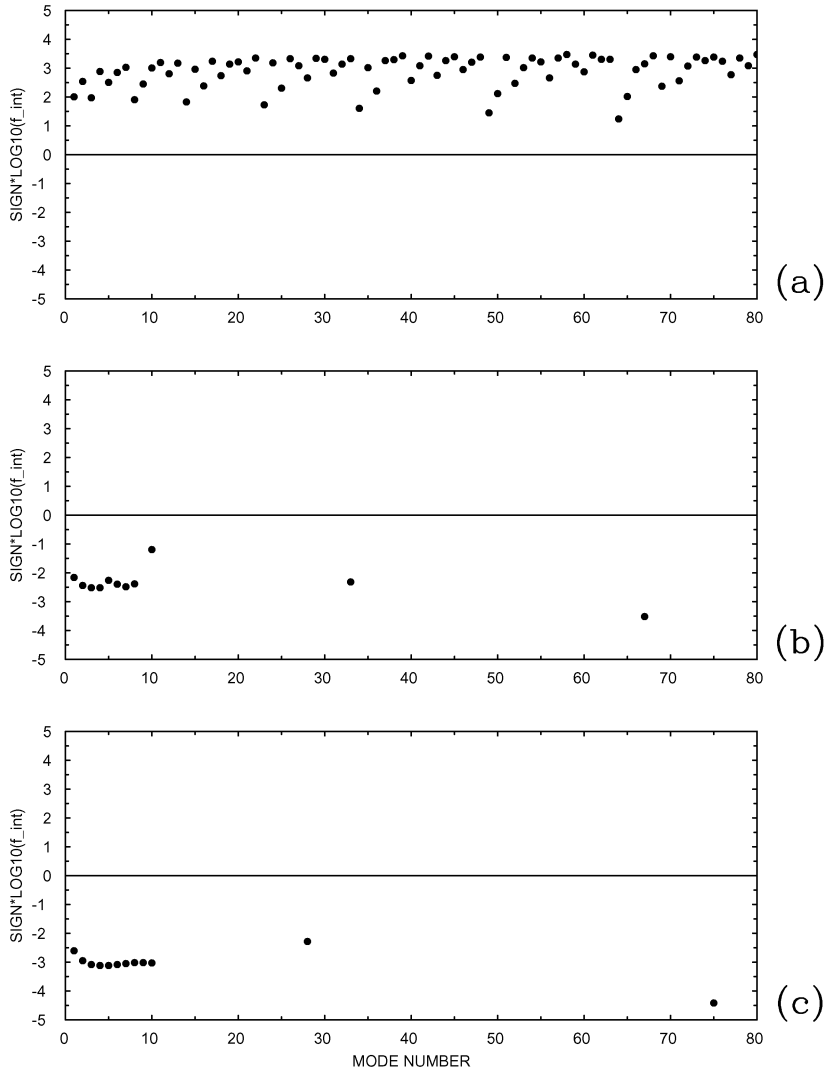

Figure 12. Average values of the eddy forcing over the southern half of the basin, F_{int}, are shown for the (a) barotropic modes, and the (b) first and (c) second baroclinic modes which have the single-cell meridional structure. First, F_{int} is taken with $10^{-6} \times \text{days}^{-2}$ units, then the logarithm of its absolute value is calculated and multiplied with the original sign: $sign(F_{int})\log_{10}|F_{int}|$.

emergence of the anti-Fofonoff gyres in the upper ocean, and the former is consistent with the Fofonoff-like gyres in Figure 4b.

In the free-slip situation and in the interior of the basin, $\langle F \rangle$ is similar to the no-slip one, but near the zonal boundaries it has no spikes. Overall, the eddy forcing does not play a substantial role in both cases, but what then drives Fofonoff gyres in the free-slip situation?

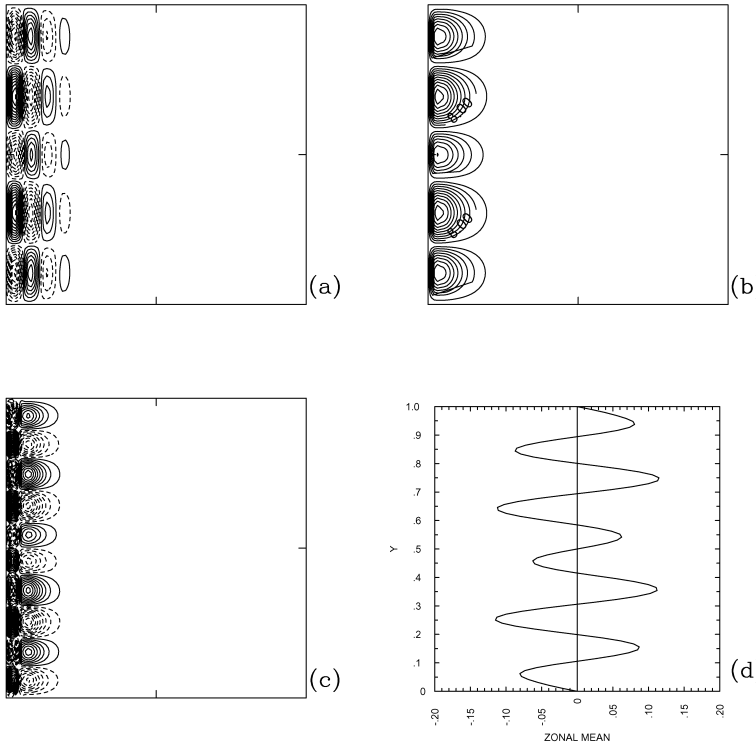

Figure 13. The same as Figure 9, but for the seventeenth mode, which is the least damped, meridionally structured mode with $n = 5$. CIs are (a) 4.0, (b) 4.0, and (c) 0.4.

Statistical-mechanics argument suggests that these gyres[5] appear as the maximum entropy solution (Salmon *et al.,* 1976). The underlying dynamical mechanism is mixing of the background planetary vorticity gradient by the barotropic basin modes. A systematic study of the associated Lagrangian mixing is beyond the scope of this paper, but would be an interesting extension of it. It is not clear what the dynamical mechanism is that enforces (18) on a population of the excited *BT*-modes, and this question is also left for the future studies. Hypothetically, this mechanism can be the mean-flow effect or the higher-order nonlinear interactions.

The meridionally structured baroclinic modes (*MS-BCL*-modes) correspond to the wedges of eigenvalues seen in Figures 8b, c, d. These eigenmodes can be grouped in terms of their meridional wavenumber, n, and one of such modes is shown in Figure 13. The modes with larger n are both more damped and have smaller values of ω_r. The *MS-BCL*-modes are characterized by short zonal scales, and therefore they are more

5. The gyres are the most pronounced with the super-slip boundary condition, which minimizes boundary fluxes of the relative vorticity to zero (Wang and Vallis, 1994).

damped than *MU-BCL*-modes with a small number of cells. The *MS-BCL*-modes are trapped near the western boundary and associated with time-dependent western-boundary intensifications. This latter can be explained with the same arguments as the asymmetry of the wind-driven gyres (Pedlosky, 1987). The eddy forcings generated by the *MS-BCL*-modes are both strong, because the modes are associated with large velocity and relative vorticity anomalies, and meridionally structured. Given all these properties, the *MS-BCL*-modes can generate zonal jets only near the western boundary, therefore they cannot explain the observed rectified jets. On the other hand, these modes can be responsible for the observed enhancement of the rectified flows near the western rather than eastern boundary (Fig. 1).

To summarize, in order to drive the observed rectified jets, a basin mode has to provide strong eddy forcing, and it has to be meridionally structured and not trapped near the western boundary. None of the above eigenmodes fully satisfies all of these conditions, so its contribution to the observed rectified jets can only be partial. On the other hand, nonlinear interactions of the least damped modes explain the emergence of the anti-Fofonoff upper-ocean gyres. Further progress is made in the next section by considering nonzero background flows.

b. Eigenmodes with non-zero-background flow

The failure of the zero-background basin modes to explain the rectified jets can be fixed by introducing the *auxiliary hypothesis:* basin modes responsible for driving the rectified jets have to be calculated with respect to the background flow given by the finite-amplitude, least-damped zero-background modes. Any direct verification of this hypothesis is problematic, because computation of the eigenmodes with respect to a time-dependent background is unfeasible for any reasonable resolution in space and time. However, some progress is made here by taking into account the slow propagation of the least damped zero-background modes. The new eigenmodes are found with respect to a background finite-amplitude mode that is kept fixed at a particular phase of its evolution. In this case amplitude and phase of the background flow are the additional parameters.

With a nonzero background flow given by the streamfunction, Ψ, and the PV anomaly, Q, the Eqs. (22)–(24) are reformulated as:

$$i\left[\nu\nabla^4\psi_1 - \beta\frac{\partial\psi_1}{\partial x} - J(\Psi_1, q_1) - J(\psi_1, Q_1)\right] = \omega(\nabla^2\psi_1 + S_1(\psi_2 - \psi_1)) \tag{30}$$

$$i\left[\nu\nabla^4\psi_2 - \beta\frac{\partial\psi_2}{\partial x} - J(\Psi_2, q_2) - J(\psi_2, Q_2)\right] = \omega(\nabla^2\psi_2 + S_{21}(\psi_1 - \psi_2) + S_{22}(\psi_3 - \psi_2)) \tag{31}$$

$$i\left[\nu\nabla^4\psi_3 - \beta\frac{\partial\psi_3}{\partial x} - J(\Psi_3, q_3) - J(\psi_3, Q_3)\right] = \omega(\nabla^2\psi_3 + S_3(\psi_2 - \psi_3)). \tag{32}$$

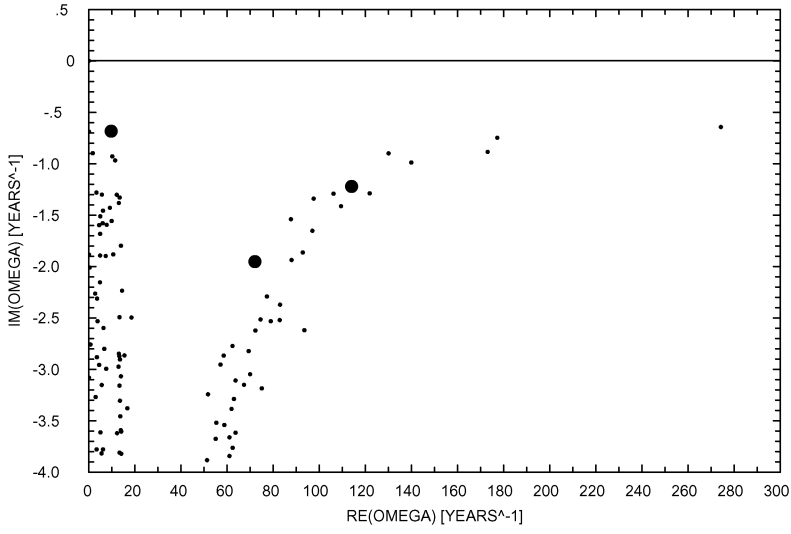

Figure 14. Eigenspectrum of the eigenmodes calculated with respect to the non-zero background flow. The large filled circles correspond to the eigenmodes shown in Figures 15, 16, and 17.

The linearized equations are reduced to the general eigenvalue problem (27), as in Section 4a, except that with the nonzero background flow the problem is no longer separable in terms of the vertical modes. Therefore, the horizontal resolution is sacrificed to 62×62 grid points in each isopycnal layer.

The background flow is chosen to be either the least damped or the second least damped, second baroclinic eigenmode, both of which are calculated in Section 4a and also diagnosed from the randomly forced solution (Section 3c). The results are qualitatively similar for either background mode. They also do not depend on phases of these modes, therefore the presentation is focused on the second mode with an arbitrarily chosen phase. Three amplitudes of the background state were tried, which correspond to the maximum meridional velocity of 0.5, 2.0, and 5.0 cm s^{-1}. The first situation is found to be rather close to the zero-background situation. The other two cases are qualitatively similar. The presentation is focused on the last case and on the top one hundred of the least damped modes. The eigenspectrum of the problem (Fig. 14) has some similarities with the zero-background spectrum, but its eigenmodes have mixed vertical structure. All of the eigenmodes are still stable, and there are no reasons to expect that their properties change significantly in the weakly unstable regime corresponding to somewhat larger background-flow amplitudes. The new eigenmodes can be sorted out into three classes which are discussed below. These classes of modes are illustrated with the particular modes marked on Figure 14.

The parasitic eigenmodes are the high-frequency modes traveling on resonant, weakly damped, zero-background basin modes (Fig. 15). They are attached to parts of the

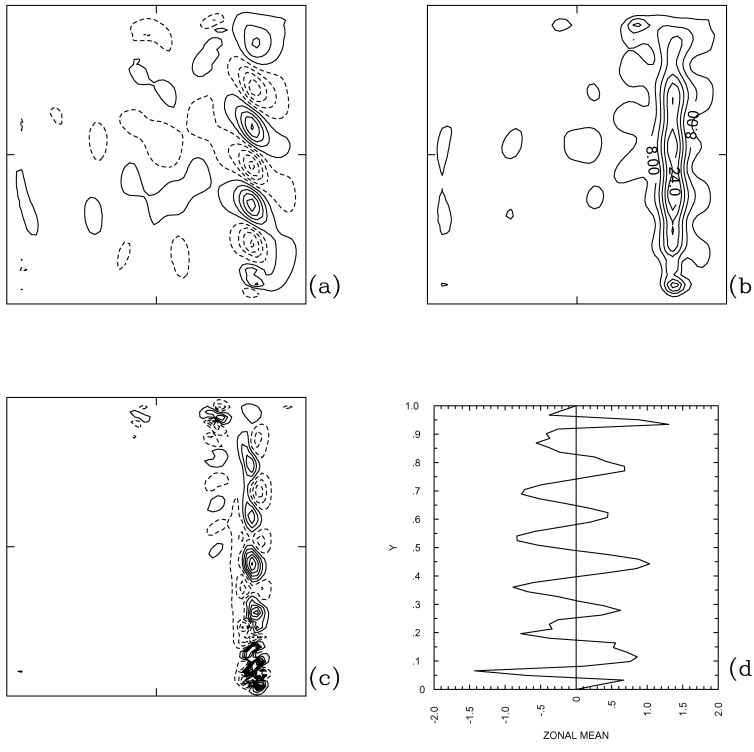

Figure 15. One of the parasitic modes, with $(\omega_r, \omega_i) = (72.10, -1.95)$ yrs^{-1}, calculated with respect to the nonzero background flow. (a) Real part, (b) amplitude, (c) upper-ocean eddy forcing, and (d) zonal mean of the upper-ocean eddy forcing. CIs are (a) 5.0, (b) 4.0, and (c) 4.0.

background flow where the vertical velocity shear is strong, therefore their amplitudes are not localized in any particular part of the basin but travel across it from east to west. The parasitic eddy forcing is very strong and meridionally finely structured. It is dominated by the isopycnal-thickness flux divergence. Thus, the parasitic modes have all the properties needed for driving rectified jets in the regimes characterized by relatively short l_m.

The second class of eigenmodes are the distorted quasi-barotropic (*DQB*) modes (Fig. 16). These are large-scale, high-frequency modes that resemble zero-background *BT*-modes. On the one hand, the *DQB*-modes have large amplitude distributed over the whole basin, as the *BT*-modes have. On the other hand, they are strongly modified by the background flow, both horizontally and vertically. In particular, the vertical distortion results in substantial isopycnal-thickness fluxes that make the eddy forcing rather strong. Given all these properties, the *DQB*-modes are also capable of driving the rectified jets.

The rest of the eigenmodes are the low-frequency modes (*LF*-modes), which have no pronounced meridional structure (Fig. 17). Their shapes are tied to the shape of the background flow, and they can be viewed as modifications of the *MU-BCL*-modes

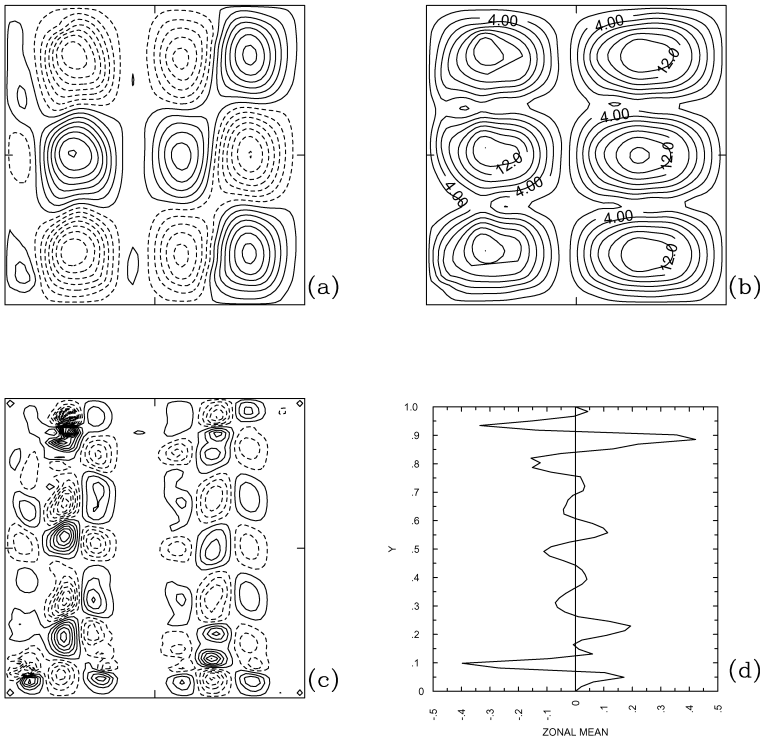

Figure 16. The same as in Figure 15, but for one of the distorted quasi-barotropic modes, with $(\omega_r, \omega_i) = (114.00, -1.22)$ yrs^{-1}. CIs are (a) 2.0, (b) 2.0, and (c) 0.5.

analyzed in the previous section. The corresponding eddy forcing patterns have large amplitudes, but they are limited to the regions just near the zonal boundaries. Given that, the *LF*-modes do not significantly contribute to the rectified jets in the interior of the basin.

5. Summary

This paper studies rectification of the large-scale oceanic flow in a closed basin on the β-plane. The flow is driven by random, zero-mean, space-time correlated forcing. The main motivation of this study is given by Berloff (2005), where it is shown that the mesoscale eddy effects on the large-scale circulation can be modeled in terms of random, space-time correlated forcing driving nonlinear, non-eddy-resolving dynamics. Another motivation comes from the observations and numerical modeling efforts that find persistent zonal jets in different parts of the global ocean.

This study focuses on an idealized basin with stratification and spatially homogeneous forcing variance. The main results can be summarized as the following.

(1) Depending on the forcing strength, two rectification regimes are found: zonal jets and isolated gyres.

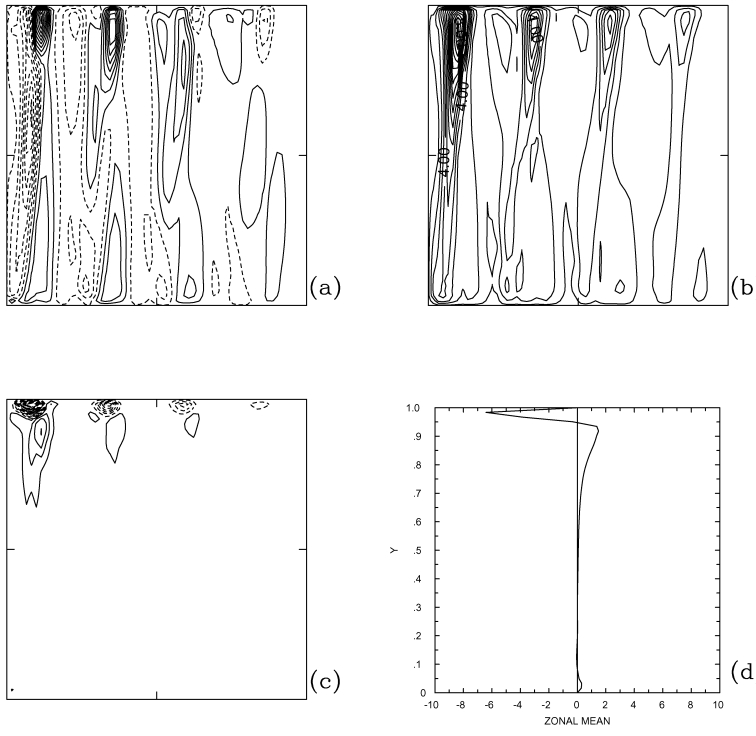

Figure 17. The same as in Figure 15, but for one of the low-frequency modes, with $(\omega_r, \omega_i) = (9.64, -0.68)$ yrs^{-1}. CIs are (a) 1.0, (b) 1.0, and (c) 4.0.

(2) It is shown that both regimes are due to nonlinear interactions of resonant basin modes.

(3) In the zonal-jet regime, these interactions involve complex interplay between resonant baroclinic modes and some secondary modes.

(4) Both Rhines' scaling for zonal jets and prediction of gyres based on the maximum entropy argument are not confirmed.

These results are based on the analysis, on the one hand, of randomly forced solutions and, on the other hand, of linear eigenmodes and their nonlinear interactions. Sensitivity of the results to parameters of the problem is studied and the main results are found robust.

The rectified jets are found for a broad range of parameters. Rhines' scaling law for the average meridional width of the jets, l_m, is tested for a broad range of parameters and not confirmed. Instead, persistent regimes characterized by preferred widths are found. Within each regime, l_m varies rather little and transitions between the regimes are relatively abrupt. It is found that l_m is rather sensitive to the beta and lateral viscosity, but not to the amplitude of the forcing, as long as the forcing variance is not very large. It is hypothesized

that the observed behaviors are due to the nonlinear self-interactions of weakly damped, resonant basin modes. Different ensembles of such modes produce different regimes, and the lower the viscosity the more significant is the contribution of the fine-structure, relatively more damped modes. Increased forcing simply fuels energy in the same excited modes, and therefore has limited impact on the rectified flow pattern.

In order to test the above hypothesis, the basin modes of the state of rest are calculated and analyzed. The modes are sorted out into three classes, none of which explains the observed jets for the following reasons. The least damped, baroclinic modes, which are also diagnosed directly from the randomly forced solutions, lack meridional structure in the interior of the basin. The barotropic modes have too weak nonlinear interactions. Finally, the meridionally structured baroclinic modes are trapped near the western boundary. Given all that, the auxiliary hypothesis is formulated, according to which rectified jets are driven by the secondary eigenmodes related not to the state of rest but to finite-amplitude background flows given by the most resonant, large-scale, zero-background eigenmodes. Direct test of this hypothesis is computationally unfeasible, but significant progress can be made by taking into account slow propagation of the background flow. Thus, the background is approximated as the steady one and its phase becomes an additional parameter. The new eigenproblem is solved and it is found that there are two new types of modes, both of which can account for the observed rectified jets, because they produce strong nonlinear interactions, effect the whole interior of the basin, and are meridionally structured. These are parasitic modes traveling on the background flow and distorted quasi-barotropic modes.

When the random forcing is strong, the isolated gyres rectify near the zonal boundaries. In the upper ocean, these gyres are characterized by the cyclone/anticyclone in the north/south, and in the deep ocean the circulation is reversed. Thus, the upper-ocean circulation is opposite to the one predicted by Fofonoff (1954) and later explained with the statistical equilibrium-mechanics arguments (Salmon *et al.,* 1976). Here, the difference is due to the flow baroclinicity which previously was not accounted for. It is shown that the upper-ocean gyres are due to nonlinear interactions of the most resonant, baroclinic basin modes of the state of rest. The deep-ocean gyres are driven by the barotropic basin modes, through their nonlinear interactions and meridional mixing of the background planetary-vorticity gradient.

The following extensions of the presented results are anticipated. Effects of time-mean flows and basin shape on the eigenmodes should be addressed. Make-up of the excited population of basin modes has to be connected with parameters of the problem. The rectification process and the role of basin modes have to be analyzed with dynamical approximations, which are less restrictive than the quasigeostrophic approximation, and with less idealized model configurations. Finally, study of the rectification needs to be broadened in order to account for the intrinsic low-frequency variability of the large-scale flow pattern.

Acknowledgments. Fruitful conversations with Joe Pedlosky are gratefully acknowledged. Suggestions made by anonymous reviewers also led to significant improvement of this work. The author is also grateful to Mary Ann Lucas for proof-reading the manuscript. Funding for this research was

provided by NSF grants OCE 0091836 and 0344094, by the Royal Society Fellowship, and by WHOI grants 27100056 and 52990035. This is WHOI contribution #11293.

APPENDIX

Random forcing

Statistical properties of the forcing are described by the autocorrelation function, R_T, isotropic horizontal correlation function, R_H, and the forcing variance, σ_f, under the assumption that the forcing statistics are Gaussian:

$$R_T(\tau) = \langle f(t) f(t+\tau) \rangle \sigma_f^{-1}, \tag{A1}$$

$$R_H(x_0, y_0, x, y) = \langle f(t, x_0, y_0) f(t, x, y) \rangle \sigma_f^{-1}, \tag{A2}$$

where $\sigma_f = \langle f^2 \rangle$, and the angle brackets indicate time averaging. Thus, deep-ocean variance, anisotropy, horizontal inhomogeneity, and intermittency of the forcing are neglected.

In the eddy-resolving model (B04), it is found that R_T has integral correlation time,

$$\theta = \int_0^\infty R_T(\tau)\, d\tau, \tag{A3}$$

which is about one week. Here, the observed $R_T(\tau)$ is approximated as

$$R_T(\tau) = \exp(-\tau/\theta), \tag{A4}$$

and the corresponding statistics are given by the first-order autoregressive process (Box *et al.,* 1994). The θ is chosen to be 10 days and the autoregressive process is integrated with the time step of 0.2 days.

Horizontal space correlations of the eddy forcing (B05) oscillate in most of the basin; in the western part they decay over several Rossby deformation scales, and in the eastern part they decay over much larger lengthscales set by transient large-scale Rossby waves. Here, for simplicity, the isotropic R_H is chosen to be monotonic and even Gaussian, with the characteristic lengthscale L_H, which is chosen to be 50 km. Here, it is found that the rectification pattern does not qualitatively depend on θ and L_H, although the larger these values are the more energetic the flow.

The following is the method for introducing space correlations in the random-forcing model. Given its covariance matrix, a space-correlated random-force vector, $\mathbf{f}$, with N degrees of freedom (for example, representing $\sqrt{N} \times \sqrt{N}$ values of a function on the space grid), is constructed from the space-uncorrelated, unit-variance noise, $\mathbf{g}$, such that:

$$\mathbf{g}\mathbf{g}^T = \mathbf{I} \tag{A5}$$

(here and below: the superscript, T, denotes transposition of the matrix, capital-letter symbols denote matrices, and $\mathbf{I}$ is the identity matrix). Here, each component of $\mathbf{g}$

corresponds to an individual, random time series generated at the corresponding grid point by an autoregressive process. Next, let's assume that there is a linear relationship,

$$\mathbf{f}(t) = \mathbf{L}\mathbf{g}(t), \tag{A6}$$

and the covariance matrix for **f** is:

$$\mathbf{C} = \langle \mathbf{f}\mathbf{f}^T \rangle. \tag{A7}$$

Then, it is found that the transformation matrix, **L**, is equal to the "square root" of the covariance matrix, which is symmetric and positive definite:

$$\mathbf{C} = \langle \mathbf{L}\mathbf{g}(\mathbf{L}\mathbf{g})^T \rangle = \langle \mathbf{L}\mathbf{g}\mathbf{g}^T\mathbf{L}^T \rangle = \mathbf{L}\langle \mathbf{g}\mathbf{g}^T \rangle \mathbf{L}^T = \mathbf{L}\mathbf{I}\mathbf{L}^T = \mathbf{L}\mathbf{L}^T. \tag{A8}$$

The transformation matrix is found by factorizing **C** with the Cholesky algorithm (Press *et al.,* 1992) and the 16-digit accuracy. Overall, the method is local rather than spectral, therefore it can be easily adapted for spatially inhomogeneous statistics.

REFERENCES

Berloff, P. 2005. Random-forcing model of the mesoscale oceanic eddies. J. Fluid Mech., *529,* 71–95.

Box, G., G. Jenkins and G. Reinsel. 1994. Time Series Analysis: Forecasting and Control, Prentice Hall, NJ, 598 pp.

Cessi, P. and S. Louazel. 2001. Decadal oceanic response to stochastic wind forcing. J. Phys. Oceanogr., *31,* 3020–3029.

Cessi, P. and F. Primeau. 2001. Dissipative selection of low-frequency modes in a reduced-gravity basin. J. Phys. Oceanogr., *31,* 127–137.

Chekhlov, A., S. Orszag, S. Sukoryansky, B. Galperin and I. Staroselsky. 1996. The effect of small-scale forcing on large-scale structures in two-dimensional flows. Physica D, *98,* 321–334.

Cummins, P. 1992. Inertial gyres in decaying and forced geostrophic turbulence. J. Mar. Res., *50,* 545–566.

Danilov, S. and D. Gurarie. 2004. Scaling, spectra and zonal jets in beta-plane turbulence. Phys. Fluids, *16,* 2592–2603.

DelSole, T. 2001. A theory for the forcing and dissipation in stochastic turbulence models. J. Atmos. Sci., *58,* 3762–3775.

Farrell, B. and P. Ioannou. 1995. Stochastic dynamics of the midlatitude atmospheric jet. J. Atmos. Sci., *52,* 1642–1656.

Fofonoff, N. 1954. Steady flow in a frictionless homogeneous ocean. J. Mar. Res., *13,* 254–262.

Griffa, A. and S. Castellari. 1991. Nonlinear general circulation of an ocean model driven by wind with a stochastic component. J. Mar. Res., *49,* 53–73.

Griffa, A. and R. Salmon. 1989. Wind-driven ocean circulation and equilibrium statistical mechanics. J. Mar. Res., *47,* 457–492.

Haidvogel, D. and P. Rhines. 1983. Waves and circulation driven by oscillatory winds in an idealized ocean basin. Geophys. Astrophys. Fluid Dyn., *25,* 1–63.

Herring, J. and R. Kraichnan. 1971. Comparison of some approximations for isotropic turbulence, *in* Statistical Models and Turbulence, M. Rosenblatt and C. van Atta, eds., Springer-Verlag, NY, 147–194.

Hogg, N. and B. Owens. 1999. Direct measurement of the deep circulation within the Brazil basin. Deep-Sea Res., *46,* 335–353.

Holloway, G. and M. Hendershott. 1977. Stochastic closure for nonlinear Rossby waves. J. Fluid Mech., *82,* 747–765.

LaCasce, J. 2002. On turbulence and normal modes in a basin. J. Mar. Res., *60,* 431–460.

LaCasce, J. and J. Pedlosky. 2004. The instability of Rossby basin modes and the oceanic eddy field. J. Phys. Oceanogr., *34,* 2027–2041.

—— 2002. Baroclinic Rossby waves in irregular basins. J. Phys. Oceanogr., *32,* 2828–2847.

Laval, J.-P., B. Dubrulle and J. McWilliams. 2003. Langevin models of turbulence: Renormalization group, distant interaction algorithms or rapid distortion theory? Phys. Fluids, *15,* 1327–1339.

Manfroi, A. and W. Young. 2002. Stability of β-plane Kolmogorov flow. Physica D, *162,* 208–232.

—— 1999. Slow evolution of zonal jets on the beta plane. J. Atmos. Sci., *56,* 784–800.

Nakano, H. and H. Hasumi. 2005. A series of zonal jets embedded in the broad zonal flows in the Pacific obtained in eddy-permitting ocean general circulation models. J. Phys. Oceanogr., *35,* 474–488.

Panetta, R. 1993. Zonal jets in wide baroclinically unstable regions: Persistence and scale selection. J. Atmos. Sci., *50,* 2073–2106.

Pedlosky, J. 1987. Geophysical Fluid Dynamics, 2nd ed., Springer-Verlag, 710 pp.

—— 1965. A study of the time dependent ocean circulation. J. Atmos. Sci., *22,* 267–272.

Preisendorfer, R. 1988. Principal Component Analysis in Meteorology and Oceanography, Elsevier, 425 pp.

Press, W., B. Flannery, S. Teukolsky and W. Vetterling. 1992. Numerical Recipes, Cambridge University Press, Cambridge, 963 pp.

Rhines, P. 1975. Waves and turbulence on a β-plane. J. Fluid Mech., *69,* 417–443.

—— 1994. Jets. Chaos, *4,* 313–339.

Ristorcelli, J. and A. Poje. 2000. Lagrangian covariance analysis of β-plane turbulence. Theoret. Comput. Fluid Dyn., *14,* 1–20.

Salmon, R., G. Holloway and M. Hendershott. 1976. The equilibrium statistical mechanics of simple quasigeostrophic models. J. Fluid Mech., *75,* 691–703.

Seidov, D. and A. Marushkevich. 1992. Order and chaos in ocean current dynamics: numerical experiments. Dyn. Atmos. Oceans, *16,* 405–434.

Smith, S. 2004. A local model for planetary atmospheres forced by small-scale convection. J. Atmos. Sci., *61,* 1420–1433.

Sura, P. and C. Penland. 2002. Sensitivity of a double-gyre ocean model to detail of stochastic forcing. Ocean Model., *4,* 327–345.

Theiss, J. 2004. Equatorward energy cascade, critical latitude, and the predominance of cyclonic vortices in geostrophic turbulence. J. Phys. Oceanogr., *34,* 1663–1678.

Treguier, A., N. Hogg, M. Maltrud, K. Speer and V. Thierry. 2003. The origin of deep zonal flows in the Brazil basin. J. Phys. Oceanogr., *33,* 580–599.

Treguier, A. and B. Hua. 1987. Oceanic quasi-geostrophic turbulence forced by stochastic wind fluctuations. J. Phys. Oceanogr., *17,* 397–411.

Vallis, G. and M. Maltrud. 1993. Generation of mean flows and jets on a beta plane and over topography. J. Phys. Oceanogr., *23,* 1346–1362.

Wang, J. and G. Vallis. 1994. Emergence of Fofonoff states in inviscid and viscous ocean circulation models. J. Mar. Res., *52,* 83–127.

Whitaker, J. and P. Sardeshmukh. 1998. A linear theory of extratropical synoptic eddy statistics. J. Atmos. Sci., *55,* 237–258.

Whitehead, J. 1975. Mean flow generated by circulation on a beta-plane: An analogy with the moving flame experiment. Tellus, *4,* 358–363.

Williams, G. 1978. Planetary circulations: 1. Barotropic representation of jovian and terrestrial turbulence. J. Atmos. Sci., *35,* 1399–1426.

Zhang, Y. and I. Held. 1999. A linear stochastic model of a GCM's midlatitude storm tracks. J. Atmos. Sci., *56,* 3416–3435.

Received: *22 June, 2004;* revised: *16 December, 2004.*